Large-area omnidirectional antireflection coating on low-index materials

Ping-Chun Li and Edward T. Yu*

Microelectronics Research Center, University of Texas at Austin, 10100 Burnet Rd., Austin, Texas 78758, USA
**Corresponding author: ety@ece.utexas.edu*

Received May 1, 2013; revised July 10, 2013; accepted August 8, 2013;
posted August 12, 2013 (Doc. ID 189830); published September 4, 2013

Large-area subwavelength dielectric hexagonal lattices of cylindrical pillars on quartz substrates that provide high optical transmittance at all angles of incidence under different polarizations of light, and are fabricated using low-cost patterning techniques, are demonstrated and analyzed. Transmittance >85% for angles of incidence in excess of 70° is demonstrated at visible and near-infrared wavelengths, and the structures employed are shown to be superior at visible wavelengths to tapered "moth eye" surfaces for practically achievable dimensions. Detailed analytical calculations and numerical simulations elucidating the impact of feature size, height, periodicity, and refractive index are presented.

OCIS codes: (170.0110) Imaging systems; (170.3010) Image reconstruction techniques; (170.3660) Light propagation in tissues.
http://dx.doi.org/10.1364/JOSAB.30.002584

1. INTRODUCTION

Coatings for reducing optical reflections from surfaces have attracted broad interest for applications ranging from photovoltaics to displays. The typical approaches for realizing antireflective surfaces can be grouped into two general categories [1]: homogeneous and inhomogeneous antireflection coatings. Homogeneous antireflection coatings typically use quarter-wave stacks of optical thin films to achieve admittance matching in both magnitude and phase [2]; however, implementations are often limited by the refractive indices of materials available in nature, although nanostructured material can expand the range of available refractive indices [3–6]. Inhomogeneous antireflection coatings can provide greater flexibility in effective refractive indices but often require the use of challenging nanofabrication processes. These have included top–down approaches such as self-masked dry etching [7], wet etching [8–11], electron beam lithography [12], interference lithography [13,14], and roll-to-roll nanoimprinting [15]; and bottom–up approaches, such as anodic alumina oxide nanoporous films [16,17], nanosphere lithography (NSL) [18], and carbon nanotubes [19]. In nearly all cases, minimizing surface reflectivity for normally incident light has been emphasized. The challenge of reducing shallow-angle (angle of incidence >60°) reflection on low-index materials has not been well addressed, in terms of both the optimization of the antireflection surface and practical limitations in fabrication over large areas. In many applications, low-index materials such as polymer and glass have been widely used as packaging material; reduced reflectivity from such surfaces at large angles of incidence can have a major practical impact, e.g., by reducing glare from a flat display monitor, or increasing total efficiency of a solar panel module.

In this paper, we report the design, fabrication, experimental characterization, and analysis of omnidirectional antireflection coatings based on subwavelength-scale hexagonal lattices of cylindrical dielectric pillars. These structures are shown to provide high optical transmittance at visible and near-infrared wavelengths for both transverse electric (TE) and transverse magnetic (TM) polarizations, with performance superior to both conventional optical thin film multilayer approaches [1,2], and to typical "moth eye" antireflection coating structures, which are shown to require extremely large depths to produce low reflectance at large angles of incidence. Theoretical and computational analyses are presented that provide insights into the conditions necessary to produce low reflectance at shallow angles under TE and TM polarizations, and fabrication via a self-assembly process is described that provides the potential for manufacture of nanostructured antireflective dielectric surfaces over large areas and at low cost.

2. EXPERIMENT

Figure 1(a) shows a schematic diagram, photograph, and scanning electron micrograph of representative omnidirectional antireflection coatings studied in this paper, along with the measurement geometries for TE and TM polarizations. The nanostructures were fabricated on 1.1 mm thick double side polished fused quartz substrates (Delta Technology). The structure of a unit cell can be specified by the hexagonal array periodicity (P), and the diameter (D) and height (h) of the constituent cylindrical dielectric pillars. Figure 1(b) shows a photo taken at shallow angle to demonstrate that the reflection from an antireflection treated substrate (left, $P = 200$ nm, $D = 90$ nm, and $h = 350$ nm) is lower than an untreated quartz substrate (right). Figure 1(c) shows the scanning electron micrograph of a fabricated structure with $P = 200$ nm, $D = 100$ nm, and $h = 350$ nm.

Figure 1(d) shows key steps in the fabrication process for the omnidirectional antireflection nanostructure. The quartz

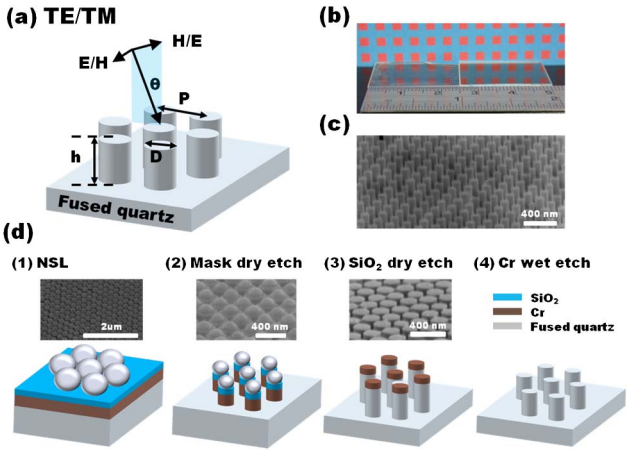

Fig. 1. (a) Schematic diagram of a dielectric hexagonal lattice structure on a quartz substrate with periodicity (P), diameter (D), height (h), and of simulation and measurement geometry for TE or TM polarization. (b) Photo taken at shallow angle, showing that the antireflection coated quartz (left, $P = 200$ nm, $D = 90$ nm, and $h = 350$ nm) is less reflective compared with the nontreated substrate (right). (c) Scanning electron micrograph of a fabricated $P = 200$ nm, $D = 100$ nm, and $h = 350$ nm structure. (d) Schematic diagram of the fabrication process flow and scanning electron micrograph at each step: (1) A quartz substrate is cleaned, covered with 60 nm Cr/10 nm SiO_2, followed by NSL using $D = 200$ nm polystyrene nanospheres. (2) A series of dry etching processes is used to transfer the hexagonal lattice pattern to the underlying Cr layer. (3) Cylindrical nanopillars formed by SiO_2 dry etching using Cr hard mask. (4) Wet etch to remove Cr.

substrate (1 square inch) is coated with 60 nm Cr/10 nm SiO_2 using e-beam evaporation. On top of the SiO_2 layer, a self-assembled ordered monolayer of 200 nm diameter polystyrene (PS) nanospheres is deposited by the Langmuir–Blodgett method. [20,21] For our implementation of this process, defect-free hexagonally close packed regions of nanospheres typically extend over distances of ~20 μm, separated by cracks between boundaries and a few vacancies. The diameters of the nanospheres are then reduced by reactive-ion etching, resulting in nanospheres with diameters of 50–150 nm, depending on etch time. These nanospheres then serve as an etch mask to transfer the hexagonal pattern to the underlying Cr, which acts as a hard mask during the subsequent quartz reactive ion etching process to achieve the desired high aspect ratio cylindrical pillar structure. Finally, the Cr mask is removed by a standard wet etch process. While the structures presented here were fabricated from quartz, the general procedure just described may be applied to other low-index materials such as soda lime glass with more specific gas reactants in dry etch to create hexagonal arrays of submicrometer- to nanometer-scale high aspect ratio pillars rapidly, at low cost, and over large areas.

Optical transmittance measurements were performed on these structures using collimated light from a halogen lamp spectrally resolved by a monochromator. The monochromatic light was linearly polarized by a Glan–Thompson polarizer before reaching the device. Devices were mounted on a rotating stage, allowing measurements to be performed at angles of incidence θ ranging from 0° to 72°. Numerical simulations of the optical behavior of these structures were performed using rigorous coupled wave analysis [22]. In these simulations, the refractive index of the quartz was taken to be 1.46, independent of wavelength.

3. RESULTS AND DISCUSSION

To achieve a wide-angle, broadband antireflection coating, theoretically an optimal graded-index profile should yield the best results [23–28]; however, such a structure would require sufficiently large depth to produce low reflectivity at large angles of incidence. As discussed below, the required depths result in structures that are highly impractical to fabricate. We have therefore focused on nanopillar structures which are physically attainable and provide wide-angle broadband antireflection properties. Theoretical calculations for single layer antireflection coatings with incident wavelength $\lambda = 500$ nm and $\theta = 85°$ can provide insight into the design of a shallow angle antireflection coating. The reflectance for such a structure, based on Fresnel's equation, can be expressed as [2]

$$R = \frac{(n_0 - n_{\text{sub}})^2\cos^2\delta + [(n_0 n_{\text{sub}}/n_{\text{arc}}) - n_{\text{arc}}]^2\sin^2\delta}{(n_0 + n_{\text{sub}})^2\cos^2\delta + [(n_0 n_{\text{sub}}/n_{\text{arc}}) + n_{\text{arc}}]^2\sin^2\delta}, \quad (1)$$

where $\delta = 2\pi\sqrt{n_{\text{arc}}^2 - \sin^2\theta}\,d/\lambda$; n_0, n_{sub}, and n_{arc} are the refractive indices of air, the dielectric substrate, and the antireflection coating layer, respectively; and d is the thickness of the antireflection coating. For a quartz substrate with $n_{\text{sub}} = 1.46$, the optimal n_{arc} can then be calculated from Eq. (1) to be 1.05 and 1.02 for TE and TM polarization, respectively, and the optimal thickness, d, can be calculated by setting $\delta = \pi/2$, yielding $d \sim 376$ nm. Materials with $n < 1.3$ do not exist in nature but we can synthesize them by fabricating a subwavelength nanostructure such as the hexagonal lattice nanopillar array illustrated in Fig. 1. We note that the effective index of a two-dimensional structure such as the nanopillar array cannot be given by an analytical closed form using effective medium theory due to difficulties in descriptions of fields along all directions [21–23]. Thus, it is necessary to determine the effective refractive index via simulations. In this retrieval process, we assume the subwavelength nanopillar structure behaves like a homogeneous medium with effective refractive index n_{eff} if $P \ll \lambda$, and we compare the simulated transmittances for nanopillar structures with different D/P ratios and a thin film with variable index n_{eff} for the same height under various angles of incidence to determine the effective refractive index at normal incidence. This process yields

$$n_{\text{eff}} \approx 0.4(D/P)^2 + 1. \quad (2)$$

The previously calculated n_{arc} can then be converted into a D/P ratio based on Eq. (2), yielding optimal values for D/P of ~0.35 and 0.22 for TE and TM polarizations respectively. Because the transmittance for TM polarization is already very high, while transmittance for TE polarization decreases rapidly with increasing angle of incidence, we choose $D/P = 0.35$ as our starting point for design and fabrication of our antireflection surfaces.

Figure 2(a) shows the numerically simulated transmittance as a function of D and P under 45° polarization with $h = 350$ nm, $\theta = 85°$, and $\lambda = 500$ nm. These simulations indicate that the transmittance can be raised to ~85%, compared to 40% for a bare quartz surface, with $D/P = 0.35$ ($n_{\text{eff}} \sim 1.05$). The optimal ratio D/P under 45° polarization is close to the previously calculated TE optimal value, since the transmittance of TE polarized light varies much more strongly than

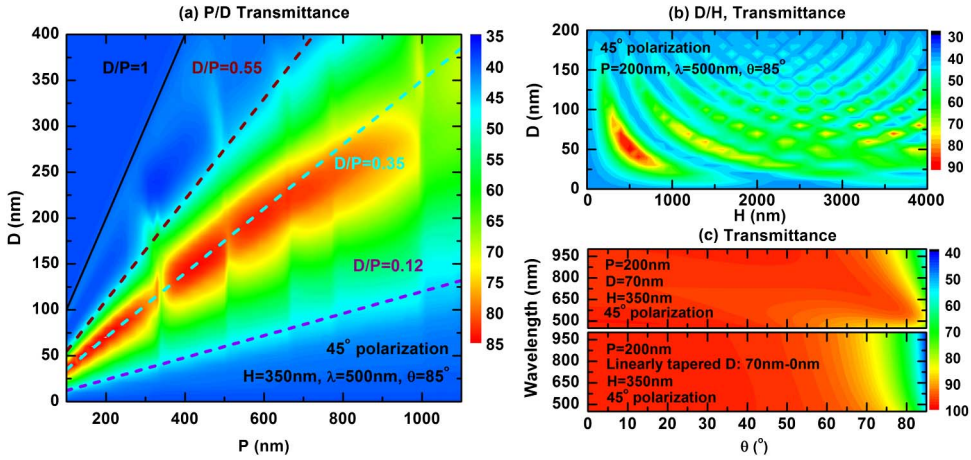

Fig. 2. Simulated transmittance spectra of a dielectric hexagonal lattice structure: (a) Transmittance contour map with $h = 350$ nm, $\lambda = 500$ nm, $\theta = 85°$ under 45° polarization. (b) Transmittance contour map with $P = 200$ nm, $\lambda = 500$ nm, $\theta = 85°$ under 45° polarization. (c) Transmittance spectra comparison between $D = 70$ nm cylindrical nanopillar structure, and linearly "moth eye" structure with tapered D from 70 to 0 nm with same $P = 200$ nm, $h = 350$ nm, under 45° polarization.

that of TM polarized light at large angles of incidence. The predicted low surface reflectance is also very robust to variations in the detailed nanopillar structure: for D/P varying from 0.12 to 0.55, or equivalently, n_{eff} varying from 1.006 to 1.12, one can still achieve ~20% (~1.5×) transmittance enhancement. In this respect, these designs are expected to be very robust to fabrication-induced variations in structure. The simulations shown in Fig. 2(a) also indicate that P can be increased to values larger than λ while maintaining high transmittance at shallow angles of incidence. However, for $P \gtrsim \lambda$, the high transmittance will result in part from higher-order diffraction peaks, and the direction of light transmittance will therefore differ from the incident direction. If the application requires only overall high transmittance regardless of diffraction, nonsubwavelength values of P can be chosen; otherwise, subwavelength periodicities are still preferred for enhancing zero-order transmission.

Figure 2(b) illustrates the simulated dependence of transmittance on D and h for P fixed at 200 nm; with $\theta = 85°$ and $\lambda = 500$ nm, the maximum transmittance can be raised to ~87.7% with $P = 200$ nm, $D = 70$ nm, and $h = 350$ nm, under 45° polarization. Away from the region of maximum transmittance, a ripple pattern associated with Fabry–Perot interferences across different values of D and h is observed: as h increases, we observe an increase in Fabry–Perot modes within the nanopillars between different D, resulting in several locally optimal points; however, these points have less tolerance to variations in the value of D/h compared with the global optimum, therefore they are less favored from a fabrication perspective. The overall transmittance decreases when D increases regardless of h, since n_{eff} increases and there is a greater mismatch between the relative refractive indices of air and substrate. The periodicity and magnitude of the Fabry–Perot interferences observed in simulation agree well with these predicted by Eq. (1).

Figure 2(c) shows a comparison of simulated transmittance spectra for angles of incidence from 0° to 85° between a tapered "moth eye" structure (for which D is linearly tapered from 70 nm to 0 nm) and the cylindrical nanopillar ($D = 70$ nm) structure, with the same period $P = 200$ nm and height $h = 350$ nm for both, under 45° polarization. The "moth eye" and cylindrical nanopillar structures have similar transmittance response (~95%) for $\theta = 0°$–$60°$; however, the transmittance of the "moth eye" structure starts to decrease quickly beyond $\theta = 60°$ while the cylindrical nanopillar structure maintains high transmittance to $\theta = 75°$ for all wavelengths, and transmittances ~80% or higher to $\theta = 80°$ in wavelength range of 500–650 nm. Our simulations can be compared with earlier experimental work of a tapered "moth-eye" structure (for which D is linearly tapered from 140 to 60 nm) with $P = 150$ nm and $h = 150$ nm on glass [23], we note that the transmittance of "moth-eye" structure with insufficient height decreases significantly when $\theta > 75°$ which is consistent with our simulations.

Perfect antireflection structures have been discussed theoretically using different tapered "moth eye" geometries [24–29]; however, the geometries of these structures need to match perfectly to form the optimally graded-index profile, and the height of the structure needs to be large enough to ensure a sufficiently smooth transition from air to substrate to avoid reflection. Therefore, both total height and potential profile imperfections are key concerns in design and fabrication of "moth eye" antireflection coatings. Figure 3(a) shows simulated transmittance spectra as a function of height (h) at $\lambda = 500$ nm and $\theta = 85°$ for an optimized cylindrical pillar structure ($D = 70$ nm, $P = 200$ nm, $h = 380$ nm) and tapered "moth eye" structures with different base diameters (D). For height h limited to 380 nm or less, the cylindrical nanopillar structure with $h = 380$ nm clearly outperforms any tapered "moth eye" structure. As the allowable height is increased to ~1 μm, certain "moth eye" structures can yield transmittance slightly higher than the cylindrical nanopillar structures but only within narrow ranges of height and base diameter. The "moth eye" structures are superior only for heights of ~1.5 μm or greater, and such structures would be both highly impractical to fabricate and very fragile in actual use. Figure 3(b) shows simulated transmittance spectra as a function of top diameter (W). The transmittance monotically decreases as the structure starts to taper. The pillar structure remains superior compared to "moth-eye" with similar dimensions until the top diameter of the pillar is decreased to 35 nm or less, providing very good tolerance to tapering due to manufacturing errors. Thus, in situations requiring very low reflectance over a broad range of angles and moderate range

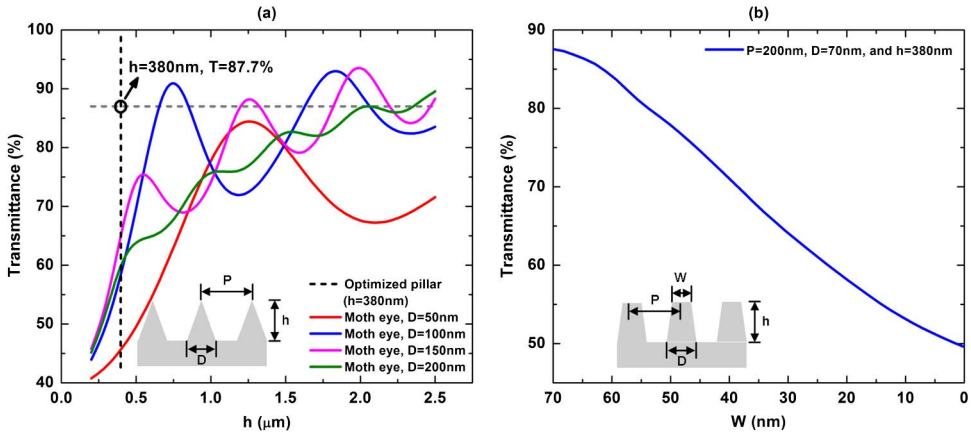

Fig. 3. (a) Simulated transmittance spectra of tapered "moth eye" structures at $\lambda = 500$ nm, $\theta = 85°$, as a function of height (h) with $P = 200$ nm and $D = 50$, 100, 150, and 200 nm under 45° polarization. The horizontal gray-dashed line corresponds to the optimized cylindrical nanopillar structure with $P = 200$ nm, $D = 70$ nm, $h = 380$ nm, and the vertical dashed line indicates $h = 380$ nm for comparison. The inset shows a schematic diagram of the tapered "moth eye" structures for which the simulations were performed. (b) Simulated transmittance spectra of tapered pillar structures with $P = 200$ nm and $D = 70$ nm at $\lambda = 500$ nm, $\theta = 85°$, as a function of top diameter (W) under 45° polarization. The inset shows a schematic diagram of the tapered pillar structures for which the simulations were performed.

of wavelengths, the cylindrical nanopillar structures demonstrated here are expected to be superior to any practical "moth eye" structure.

Figure 4(a) shows the measured transmittance spectra for nanopillar structures with $P = 200$ nm, $h = 350$ nm, and $D = 50$, 90, or 100 nm, along with transmittance for an unpatterned quartz substrate, for $\theta = 0° - 72°$ and $\lambda = 450$–1050 nm, under TE polarization. The transmittances for nanopillar structures with $D = 50$, 90, and 100 nm are greatly enhanced compared to that for the quartz substrate for all wavelengths and angles of incidence. Figure 4(b) shows a comparison of different transmittance spectra with $\lambda = 500$ nm, at $\theta = 0° - 85°$. Within these structures, $D = 90$ nm shows the highest transmittance (~87%) at $\theta = 72°$, which is ~25% (~1.45×) enhancement in transmittance compared with the unpatterned quartz substrate; the

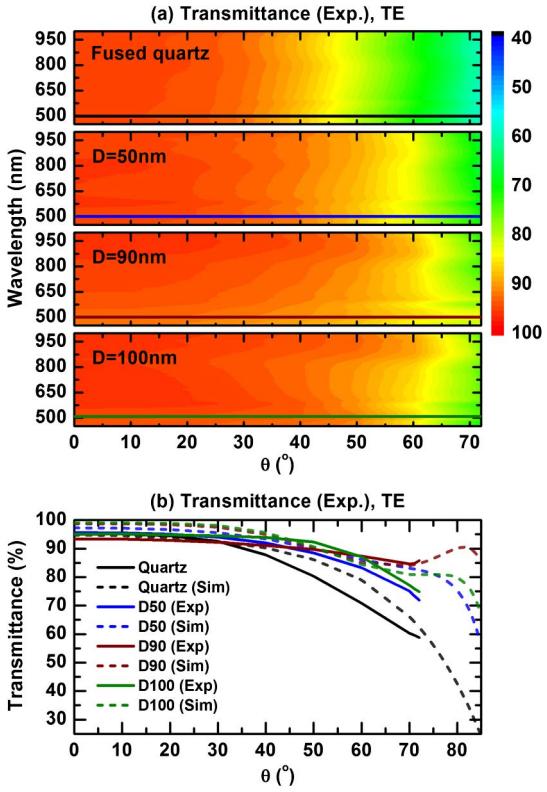

Fig. 4. (a) Measured transmittance spectra of quartz, and cylindrical nanopillar structures with $P = 200$ nm, $h = 350$ nm, and $D = 50$, 90, or 100 nm. (b) Measured (solid lines) and simulated (dashed lines) transmittances at $\lambda = 500$ nm, as functions of angle of incidence (θ) for quartz substrate and structures with $P = 200$ nm, $h = 350$ nm, and $D = 50$, 90, or 100 nm under TE polarization.

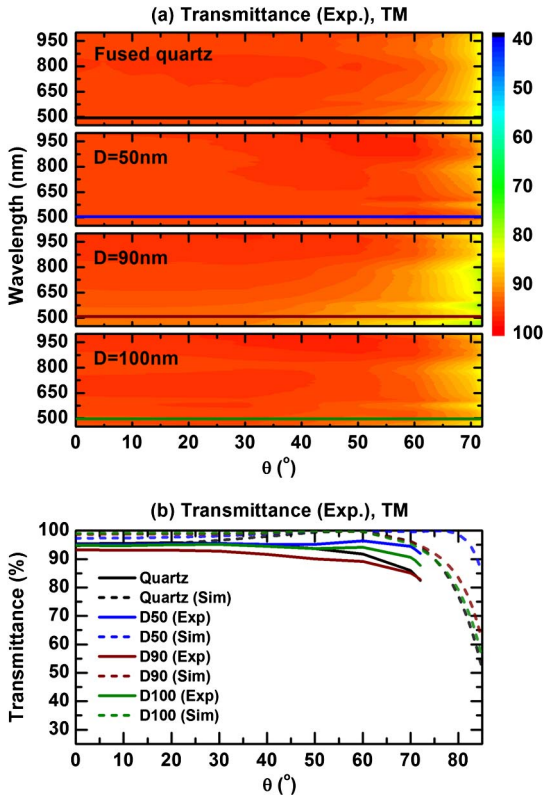

Fig. 5. (a) Measured transmittance spectra of quartz, and cylindrical nanopillar structures with $P = 200$ nm, $h = 350$ nm, and $D = 50$, 90, or 100 nm. (b) Measured (solid lines) and simulated (dashed lines) transmittances at $\lambda = 500$ nm, as functions of angle of incidence (θ), for quartz substrate and structures with $P = 200$ nm, $h = 350$ nm, and $D = 50$, 90, or 100 nm under TM polarization.

transmittance spectra of structures with $D = 50$ and 100 nm show similar enhancement, but of slightly smaller magnitude than for $D = 90$ nm, due to the nonoptimal D/P ratio.

Figure 5(a) shows the measured transmittance spectra under TM polarization. The transmittances of the cylindrical nanopillar structures with $D = 50$ and 100 nm are ~92%, which is similar to that of the unpatterned quartz substrate for $\theta = 0°$–$50°$, and reaches ~95%, which is higher than that for the unpatterned surface, when $\theta > 50°$. Transmittance for $D = 90$ nm is close to that of the unpatterned substrate since the admittance is slightly less optimized at TM polarization, but given the large TE transmittance this structure exhibits at shallow angles, the overall transmittance for the $D = 90$ nm structure averaged over all incident polarizations will be the highest. The simulations are generally in good agreement with experimental data except for a small offset, which we attribute to fabrication imperfections and differences in dispersion relations between the actual quartz substrate and the values assumed in our simulation.

4. CONCLUSIONS

In summary, we have designed, demonstrated, and analyzed a series of subwavelength dielectric nanostructures that provide very high transmittance over visible wavelengths for different polarizations and over the entire range of angle of incidence. Detailed analysis based on simulations and theory reveal the optimal choices of feature size, periodicity, and height of subwavelength nanopillar structures associated with matching of phase and magnitude at large angle of incidence. The performance of an optimal nanopillar structure is shown to be superior to that of "moth eye" structures within realistic fabrication limits on low-index substrates. The nanopillar structures fabricated via NSL are tunable, may be applicable to different substrates, and can be used for a broad range of practical applications.

ACKNOWLEDGMENTS

Part of this work was supported by the National Science Foundation (ECCS-1128682 and ECCS-1120823) and the Judson S. Swearingen Regents Chair in Engineering at the University of Texas at Austin. P.-C. Li would like to thank H.-H. Kung (Rutgers University) for detailed discussions on NSL and E.-S. Liu (UT-Austin) for fruitful discussions and inspirations on fabrication process.

REFERENCES

1. J. A. Dobrowolski, D. Poitras, P. Ma, H. Vakil, and M. Acree, "Toward perfect antireflection coatings: numerical investigation," Appl. Opt. **41**, 3075–3083 (2002).
2. H. A. Macleod, *Thin-Film Optical Filters* (CRC Press, 2010).
3. J. Q. Xi, M. F. Schubert, J. K. Kim, E. F. Schubert, M. Chen, S.-Y. Lin, W. Liu, and J. A. Smart, "Optical thin-film materials with low refractive index for broadband elimination of Fresnel reflection," Nat. Photonics **1**, 176–179 (2007).
4. M.-L. Kuo, D. J. Poxson, Y. S. Kim, F. W. Mont, J. K. Kim, E. F. Schubert, and S.-Y. Lin, "Realization of a near-perfect antireflection coating for silicon solar energy utilization," Opt. Lett. **33**, 2527–2529 (2008).
5. R. E. Welser, A. W. Sood, G. G. Pethuraja, A. K. Sood, Y. Xing, D. J. Poxson, C. Jaehee, E. F. Schubert, and J. L. Harvey, "Broadband nanostructured antireflection coating on glass for photovoltaic applications," in *38th IEEE Photovoltaic Specialists Conference (PVSC)* (IEEE, 2012), p. 003339.
6. J.-Y. Cho, K.-J. Byeon, and H. Lee, "Forming the graded-refractive-index antireflection layers on light-emitting diodes to enhance the light extraction," Opt. Lett. **36**, 3203–3205 (2011).
7. Y.-F. Huang, S. Chattopadhyay, Y.-J. Jen, C.-Y. Peng, T.-A. Liu, Y.-K. Hsu, C.-L. Pan, H.-C. Lo, C.-H. Hsu, Y.-H. Chang, C.-S. Lee, K.-H. Chen, and L.-C. Chen, "Improved broadband and quasi-omnidirectional anti-reflection properties with biomimetic silicon nanostructures," Nat. Nanotechnol. **2**, 770–774 (2007).
8. P. Menna, G. Di Francia, and V. La Ferrara, "Porous silicon in solar cells: a review and a description of its application as an AR coating," Solar Energy Mater. Solar Cells **37**, 13–24 (1995).
9. W. Theiß, "Optical properties of porous silicon," Surf. Sci. Rep. **29**, 91–192 (1997).
10. C. C. Striemer and P. M. Fauchet, "Dynamic etching of silicon for broadband antireflection applications," Appl. Phys. Lett. **81**, 2980–2982 (2002).
11. J. Y. Chen and K. W. Sun, "Nanostructured thin films for antireflection applications," Thin Solid Films **519**, 5194–5198 (2011).
12. S. A. Boden and D. M. Bagnall, "Tunable reflection minima of nanostructured antireflective surfaces," Appl. Phys. Lett. **93**, 133108 (2008).
13. P. B. Clapham and M. C. Hutley, "Reduction of lens reflexion by the moth eye principle," Nature **244**, 281–282 (1973).
14. K.-C. Park, H. J. Choi, C.-H. Chang, R. E. Cohen, G. H. McKinley, and G. Barbastathis, "Nanotextured silica surfaces with robust superhydrophobicity and omnidirectional broadband supertransmissivity," ACS Nano **6**, 3789–3799 (2012).
15. N. Yamada, T. Ijiro, E. Okamoto, K. Hayashi, and H. Masuda, "Characterization of antireflection moth-eye film on crystalline silicon photovoltaic module," Opt. Express **19**, A118–A125 (2011).
16. Y. Kanamori, K. Hane, H. Sai, and H. Yugami, "100 nm period silicon antireflection structures fabricated using a porous alumina membrane mask," Appl. Phys. Lett. **78**, 142–143 (2001).
17. H. Deniz, T. Khudiyev, F. Buyukserin, and M. Bayindir, "Room temperature large-area nanoimprinting for broadband biomimetic antireflection surfaces," Appl. Phys. Lett. **99**, 183107 (2011).
18. W. Zhou, M. Tao, L. Chen, and H. Yang, "Microstructured surface design for omnidirectional antireflection coatings on solar cells," J. Appl. Phys. **102**, 103105 (2007).
19. Z.-P. Yang, L. Ci, J. A. Bur, S.-Y. Lin, and P. M. Ajayan, "Experimental observation of an extremely dark material made by a low-density nanotube array," Nano Lett. **8**, 446–451 (2008).
20. J. Rybczynski, U. Ebels, and M. Giersig, "Large-scale, 2D arrays of magnetic nanoparticles," Colloids Surf. A **219**, 1–6 (2003).
21. C.-C. Ho, P.-Y. Chen, K.-H. Lin, W.-T. Juan, and W.-L. Lee, "Fabrication of monolayer of polymer/nanospheres hybrid at a water-air interface," ACS Appl. Mater. Interfaces **3**, 204–208 (2011).
22. M. G. Moharam and T. K. Gaylord, "Rigorous coupled-wave analysis of planar-grating diffraction," J. Opt. Soc. Am. **71**, 811–818 (1981).
23. Y. Kanamori, H. Kikuta, and K. Hane, "Broadband antireflection gratings for glass substrates fabricated by fast atom beam etching," Jpn. J. Appl. Phys. **39**, L735–L737 (2000).
24. M. Chen, H.-C. Chang, A. S. P. Chang, S.-Y. Lin, J. Q. Xi, and E. F. Schubert, "Design of optical path for wide-angle gradient-index antireflection coatings," Appl. Opt. **46**, 6533–6538 (2007).
25. W. H. Southwell, "Pyramid-array surface-relief structures producing antireflection index matching on optical surfaces," J. Opt. Soc. Am. A **8**, 549–553 (1991).
26. D. H. Raguin and G. M. Morris, "Antireflection structured surfaces for the infrared spectral region," Appl. Opt. **32**, 1154–1167 (1993).
27. E. B. Grann, M. G. Moharam, and D. A. Pommet, "Artificial uniaxial and biaxial dielectrics with use of two-dimensional subwavelength binary gratings," J. Opt. Soc. Am. A **11**, 2695–2703 (1994).
28. E. B. Grann, M. G. Varga, and D. A. Pommet, "Optimal design for antireflective tapered two-dimensional subwavelength grating structures," J. Opt. Soc. Am. A **12**, 333–339 (1995).
29. L. Tsakalakos, Y. A. Xi, B. A. Korevaar, T. R. Tolliver, and D. Zhong, "Nanostructured anti-reflection coatings and associated methods and devices," U.S. patent application 2010/0259823 A1 (October 14, 2010).